Tumor-targeting multi-shelled hollow nanospheres as drug loading platforms for imaging-guided combinational cancer therapy

Wang, Wentao; Zheng, Tao; Zhang, Ming; Zhang, Qicheng; Wu, Fan; Liu, Yihan; Zhang, Lin; Zhang, Jun; Wang, Mingqian; Sun, Yi

Published in:
Biomaterials Science

Link to article, DOI:
10.1039/c9bm01881f

Publication date:
2020

Document Version
Peer reviewed version

Tumor-Targeting Multi-shelled Hollow Nanospheres as Drug Loading Platforms for Imaging-Guided Combinational Cancer Therapy

Wentao Wang[a,c+], Tao Zheng[a+], Ming Zhang[a,c*], Qicheng Zhang[c], Fan Wu[c], Yihan Liu[c], Qian Zhang[d], Jun Zhang[c], Mingqian Wang[b*], Yi Sun[a*]

[a]*Department of Health Technology, Technical University of Denmark, Kongens Lyngby, 2800, Denmark;*
[b]*Jiangsu Collaborative Innovation Center for Biomedical Functional Materials, School of Chemistry and Materials Science, Nanjing Normal University, Nanjing 210023, China;*
[c]*Wuxi Children's Hospital, Wuxi, 210023, China;*
[d]*Key Laboratory of High Performance Polymer Material and Technology of Ministry of Education, School of Chemistry and Chemical Engineering, Nanjing University, Nanjing, 210023, China*

Corresponding authors: Ming Zhang, mzhan@dtu.dk; Yi Sun, suyi@dtu.dk
[+]These authors contributed equally to this work.

Abstract

In this work, we developed multi-shelled hollow nanospheres [RGD@a_m-ZnO@CuO@Au@DOX HNSs] as multifunctional therapeutic agents to achieve effective and targeted Zn^{2+}/Cu^{2+} therapy, induced drug delivery under pH/red-light, and enhanced phototherapy under single red-light. The photothermal and photodynamic performance of the a_m-ZnO@CuO@Au HNSs was enhanced relative to that of a_m-ZnO nanoparticles (NPs) or a_m-ZnO@CuO HNSs by utilizing the resonance energy transfer process and broad red-light absorption. The pH-sensitive a_m-ZnO@CuO@Au HNSs were dissolved to Zn^{2+}/Cu^{2+} in acidic endosome/lysosome of cancer cells, resulting in a cancer cell killing effect. Releasing performance of doxorubicin (DOX) from the RGD@a_m-ZnO@CuO@Au@DOX HNSs was evaluated under low pH and red-light-irradiated conditions, and targeting of HNSs was confirmed by dual-modal imaging (magnetic resonance/fluorescence) of

the tumor area. Moreover, *in vivo* synergistic therapy using the RGD@a_m-ZnO@CuO@Au@DOX HNSs was further evaluated in the mice bearing human pulmonary adenocarcinoma (A549) cells tumors, achieving a remarkable synergistic antitumor effect superior to that obtained by monotherapy. This study validated that RGD@a_m-ZnO@CuO@Au@DOX HNSs can offer a promising candidate for efficient postoperative cancer therapy.

Keywords: multifunctional therapeutic agents, chemotherapy, photothermal, photodynamic, magnetic resonance, synergistic therapy

1. Introduction

Phototherapy, including photodynamic therapy (PDT) and photothermal therapy (PTT), is a more effective method for treating tumors compared with chemotherapy, especially in the treatment of superficial tumors [1-3]. Red-light-triggered phototherapy further provides a promising strategy for the removal of deep tumors [4]. The phototherapy has been favored by scientists in recent years due to its minimal requirements for equipment, low cost, easy to operate and control, as well as minimal damage to normal tissues [5]. However, monotherapy usually fails to achieve a satisfactory therapeutic outcome. By contrast, the combination of phototherapy and chemotherapy, as chemophototherapy, can enhance anticancer efficacy through synergistic effects [6,7]. Phototherapy can potentiate therapeutic effects by improving drug accumulation in the tumor, while chemotherapy can inhibit cell proliferation and promoting cell apoptosis, which usually occurs after phototherapy [8,9]. Therefore, chemophototherapy is an emerging and powerful technique for various cancer treatments. Considerable efforts have been exerted for the development of light-triggered nanomaterials with simultaneous PTT and PDT effects. Therefore, several PTT/PDT nanosystems, such as gold nanoparticles (AuNPs) [10], carbon quantum dots (CQDs) [11], black phosphorus quantum dots (BPQDs) [12], WS_2 NPs [13], and MoS_2 nanosheets [14,15] have been combined with typical inorganic semiconductors (such as CuO NPs [16], CuS NPs [17], Cu_2S NPs [18], Cu_2O NPs

[19], and ZnO NPs [20]) through encapsulation or surface fixation to construct PTT/PDT therapeutic agents [21-23]. In principle, the effect of inorganic semiconductors on apoptosis induction is closely related to reactive oxygen species (ROS) production and depends on the presence of defect sites in the structures of inorganic semiconductors [24]. Also, Doxorubicin (DOX) could selectively be loaded onto the surface of nanoparticles via formation of (π-π) stacking, electrostatic interactions, and metal-DOX complex [23,25]. Therefore, we need to develop new biocompatible carrier materials and develop more innovative methods to fabricate synergetic therapeutic agents.

Diverse nanoplatforms have been designed as potosensitizers for enhancing the PDT effect. Most of these nanosystems were based on the loading of inorganic semiconductors into one NPs. Especially, inorganic ZnO and CuO NPs have also been explored for PDT [19,20,26]. As we know, ZnO NPs possessed three features: (1) exert distinct effects on mammalian cell viability, (2) rapidly proliferative cancer cells are highly susceptible, and (3) quiescent cells or normal cells are less sensitive [26]. Therefore, ZnO NPs were easily internalized into the cells via electrostatic interaction, generating ROS to cause cell death [27]. Doping ZnO with CuNPs, AuNPs, or MgNPs slightly increases the activity of nanosized ZnO to produce ROS. The enhanced activity of doped metal oxides was due to their increased structural defects [20,28,29]. Among them, AuNPs are preferred due to their high absorption ability in the NIR region for PTT and excellent biocompatibility [30]. Additionally, Zn^{2+} penetrates cells and damage cellular components, such as DNA and proteins, which are toxic and may cause cell death [31,32]. The AuNPs decorated on ZnO NPs are a new therapeutic agent for PDT, PTT and Zn^{2+} therapy have not yet been reported.

Moreover, CuO NPs have also attracted much attention because of their promising photodynamic properties [33]. CuO NPs have intrinsic copper vacancies in the lattice, which affords the localized surface plasmon resonance (LSPR) in the red-light region, and thus a large number of hole carriers can be induced [34,35]. The photodynamic properties of CuO NPs, given their abundant hole carriers, probably

originate from the hydroxyl radicals (•OH) formed through the reaction between the hole and H_2O molecules [36]. However, CuO NPs still suffer from a relatively low light conversion efficiency, and they cannot generate a satisfactory therapeutic outcome for clinical use; thus, their cancer treatment application is limited. Recently, the integration of CuO into plasmonic noble metal nanomaterials is emerging as a promising approach for enhancing photothermal performance through the LSPR coupling effect between CuO and a noble metal [37]. Although, Cu-based nanosystems have been reported in the field of cancer therapy [38], the exploration of efficient CuO-mediated PDT nanomaterials remains a great challenge. CuO NPs can be rapidly transformed into Cu^{2+} by acidic endosomes/lysosomes [39]. Cu^{2+} exhibits significant cytotoxic effects only after dissolution and preferentially kills cancer cells [40]. Au@CuO hybrid nanosystems, owing to their stability and biodegradability, could be successfully used as therapeutic reagents for PDT, PTT, and Cu^{2+} therapy.

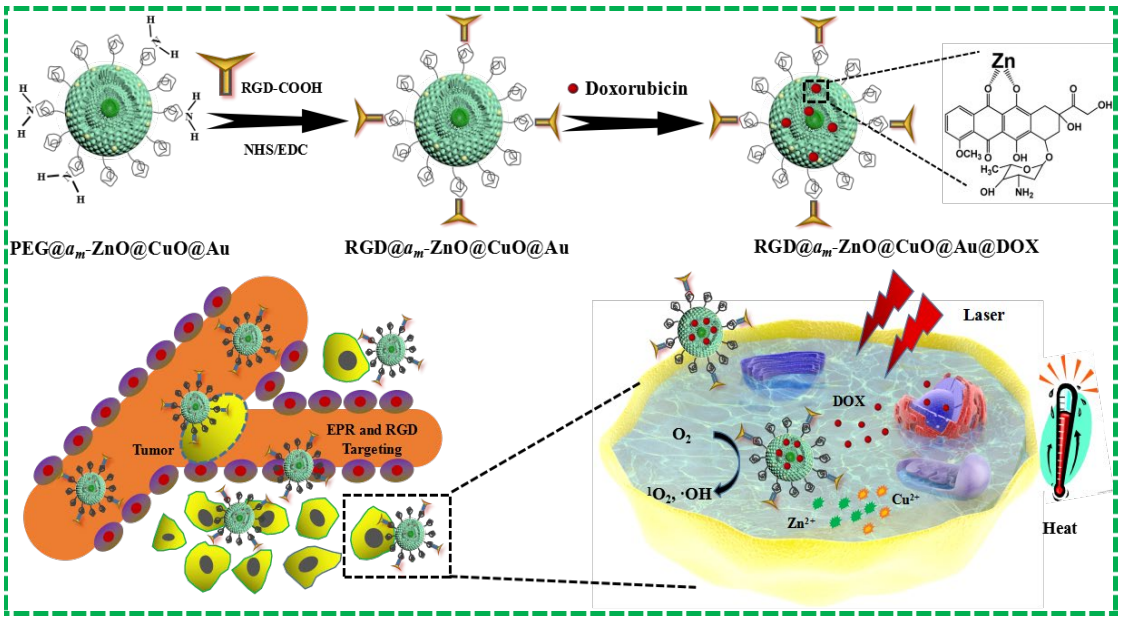

Scheme 1. Schematic for the preparation and antitumor mechanism of RGD@a_m-ZnO@CuO@Au@DOX HNSs.

Herein, we reported an efficient, multifunctional therapeutic agent-doxorubicin-loaded, RGD peptide-conjugated, and PEGylated a_m-ZnO@CuO@Au hollow nanospheres [RGD@a_m-ZnO@CuO@Au@DOX HNSs], which can target and kill cancer cells by Zn^{2+}/Cu^{2+} therapy, chemotherapy, and

phototherapy. As shown in Scheme 1., a_m-ZnO@CuO HNSs were used to generate ROS through photoexcitation, which irreversibly damaged the target of interest. AuNPs emitted a strong LSPR band in the red-light region for photothermal conversion, enhanced ROS generation, and DOX release. RGD peptides served as markers for cancer cell targeting, and DOX served as a chemotherapeutic agent. Moreover, Cu^{2+} ions offered a strong contrast in T_1-weighted magnetic resonance (MR) imaging. Targeting was confirmed by MR and fluorescence images, and the release behavior of DOX was evaluated under low pH and red-light irradiation. The present study demonstrated the promising use of a_m-ZnO@CuO HNSs as innovative semimetal nanoplatforms for theranostic delivery, and evaluated the therapeutic effect of RGD@a_m-ZnO@CuO@Au@DOX HNSs, thereby providing insights into semimetal NPs.

2. Results and discussion

2.1 Preparation of a_m-ZnO@CuO@Au HNSs

The synthetic procedure of a_m-ZIF and a_m-ZIF@Cu@Au NPs was similar to the reported method [41], as shown in Figure S1-S6. a_m-ZIF@Cu@Au NPs could serve as a spherical precursor to fabricate a multi-shelled HNSs and binary oxide a_m-ZnO@CuO@Au NPs. As shown in the transmission electron microscopy (TEM) and high-resolution TEM (HRTEM) images (Figure 1A and Figure S7), well-defined triple-shelled HNSs were produced after calcining the a_m-ZIF@Cu@Au NPs powder at 280 °C for 1.0 h, and each porous shell was formed from tiny crystallites (with pore size of about 12 nm, and BET surface area of 131.4 m^2/g; Figure S8). Compared with the original a_m-ZIF@Cu@Au NPs, the NPs sizes of the multishelled product became smaller with an average size of ca. 395 nm. Energy dispersive spectrometer (EDS) elemental maps (Figure 1B) and EDS spectrum (Figure S9) confirmed the homogeneous mixture of Cu, Au, and Zn elements in all the shells. Element analysis for the overall composition of the resultant a_m-ZnO@CuO@Au HNSs was characterized via X-ray photoelectron spectroscopy (XPS) (Figure S10), showing the

contents of Au (1.25 wt%), Cu (0.98 wt%), and Zn (3.41 wt%). The XPS scans of the O 1s (Figure 1C) and Cu $2p_{3/2}$ peaks (Figure S11) revealed that the binding energies were consistent with CuO NPs. The metallic states of Zn (Figure S12A) and Au (Figure S12B) were also confirmed via XPS. Crystalline structures of Au, ZnO, and CuO were further examined using X-ray powder diffraction (XRD) pattern (Figure 1D), showing the cubic phase of Au, hexagonal-phased of ZnO, and monoclinic-phased of CuO.

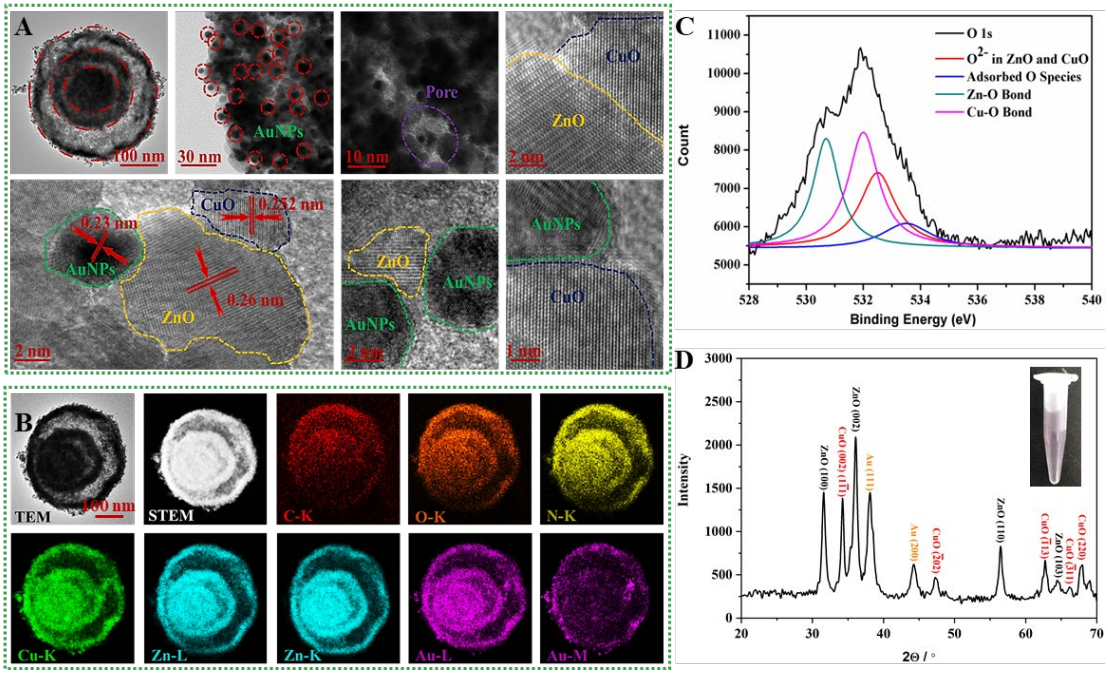

Figure 1 (A) TEM and HRTEM image of a_m-ZnO@CuO@Au HNSs. (B) TEM-EDS elemental mapping images of a_m-ZnO@CuO@Au HNSs. (C) The high resolution O1s spectra of a_m-ZnO@CuO@Au HNSs. (D) XRD spectrum of a_m-ZnO@CuO@Au HNSs.

2.2 Photodynamic property of a_m-ZnO@CuO@Au HNSs

4-oxo-2,2,6,6-tetramethylpiperidine (4-oxo-TEMP) and 5-tertbutoxycarbonyl-5-methyl-1-pyrroline N-oxide (BMPO) were used to test singlet oxygen ($^1O_2$) and hydroxyl radical (·OH), respectively. Besides, for ROS confirmation, we examined the ·OH and $^1O_2$ scavenging by DMSO and NaN_3. Figure S13 illustrated the means used in this research to identify and distinguish the generation of reactive oxygen species (ROS) during NPs photoexcitation. Figure 2A

shows the electron paramagnetic resonance spectrometer (ESR) spectra of the solutions with various spin probes and a_m-ZnO NPs, a_m-ZnO@CuO NPs, a_m-ZnO@Au NPs, and a_m-ZnO@CuO@Au HNSs before and during exposed with red-light. No ESR signal could be found in the control samples (the spin probe and samples without irradiation). BMPO was selected to verify the ·OH generation induced by a_m-ZnO NPs, a_m-ZnO@CuO NPs, a_m-ZnO@Au NPs, and a_m-ZnO@CuO@Au HNSs. Upon exposure in the presence of a_m-ZnO NPs, four-line spectrum could be found which was the characteristic spectrum of the adduct generated from BMPO/·OH. When a_m-ZnO@Au NPs and a_m-ZnO@CuO@Au HNSs were added, the BMPO/·OH signal intensity increased obviously with that of pure a_m-ZnO and a_m-ZnO@CuO NPs. These results indicated that ·OH was produced from a_m-ZnO@Au NPs and a_m-ZnO@CuO@Au HNSs during irradiation, and the existence of Au on ZnO and CuO effectively enhanced the photogeneration of ·OH. The scavenging effect of DMSO was studied on the ESR signal from a_m-ZnO NPs, a_m-ZnO@CuO NPs, a_m-ZnO@Au NPs, and a_m-ZnO@CuO@Au HNSs to estimate whether the ESR signal came from the ·OH. As expected, when photoexcited a_m-ZnO@Au NPs and a_m-ZnO@CuO@Au HNSs were the sources for ·OH generation, we found that the addition of 10% DMSO resulted in the significant reduction of ·OH (Figure 2B). These results indicated that ·OH was generated during a_m-ZnO@Au **NPs** and a_m-ZnO@CuO@Au HNSs irradiation.

Additionally, 4-Oxo-TEMP was chosen as a spin probe for studying the improved result of AuNPs on $^1O_2$ generation. 4-Oxo-TEMP itself was ESR silent. There was no ESR signal for the spin probe and samples without irradiation. A triplet spectrum, which is a characteristic of the combination between $^1O_2$ and spin probe, was found after irradiation of a_m-ZnO NPs, a_m-ZnO@CuO NPs, a_m-ZnO@Au NPs, and a_m-ZnO@CuO@Au HNSs (Figure 2A). The ESR spectrum verified the generation of $^1O_2$. The ESR signal that resulted from $^1O_2$ was confirmed by testing a $^1O_2$ scavenger (sodium azide). The triplet ESR spectrum had an obvious decrease when a_m-ZnO NPs, a_m-ZnO@CuO NPs, a_m-ZnO@Au NPs, and a_m-ZnO@CuO@Au

HNSs under irradiation in the presence of NaN_3, demonstrating the previous observation that $^1O_2$ was produced. For the same experimental condition, the generation of ESR signals intensity from photoexcited a_m-ZnO@Au NPs and a_m-ZnO@CuO@Au HNSs were about 5 and 8 times higher than that from a_m-ZnO and a_m-ZnO@CuO NPs (Figure 2C), proving that the existence of Au on ZnO and CuO could enhance $^1O_2$ generation. And in Figure 2D, we gave the mimic diagrams about the generation of ROS from a_m-ZnO@CuO@Au HNSs under 635 nm laser irradiation.

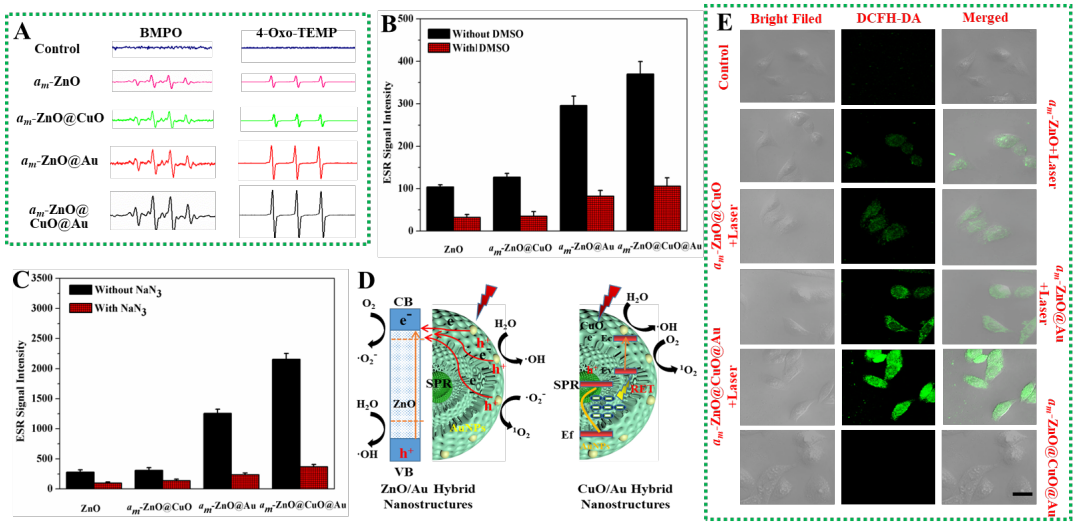

Figure 2. (A) ESR spectra (BMPO as a spin trap for the ·OH, 4-Oxo-TEMP for $^1O_2$ test) of a_m-ZnO@CuO@Au HNSs under 635 nm laser irradiation. (B) Influence of DMSO on ESR signal generated from a_m-ZnO@CuO@Au HNSs. (C) Influence of NaN_3 on ESR signal intensity from spin-label 4-Oxo-TEMP in the presence of a_m-ZnO@CuO@Au HNSs. (D) Schematic illustration of a_m-ZnO@CuO@Au HNSs for ROS generation under 635 nm laser irradiation. (E) CLSM images of DCFH-DA-stained A549 cells in the presence of different samples. Size bar = 20 μm.

The aforementioned tested results were our assessments of what specimens were *in vitro*, and the photodynamic effect in cancer cells was appraised by using an oxidative stress-sensitive dye, a ROS-index probe, 2,7-dichlorofluorescin diacetate (DCFH) [6]. DCFH could be oxidized to DCF by ROS and presenting green fluorescence excited at 520 nm. In Figure 2E, the incubation of ultrathin a_m-ZnO@CuO@Au HNSs without light exposure showed no green fluorescence of DCF, while inordinately bright green fluorescence was observed in cells after light

exposure, indicating that ROS in the cells the ROS was generated inside cells after irradiation. HeLa cells dealt with a_m-ZnO NPs, a_m-ZnO@CuO NPs, and a_m-ZnO@Au NPs upon 635 nm irradiation exhibited weak green fluorescence, whereas the cells incubated with PBS showed a nearly invisible color, indicating that ZnO/CuO can produce ROS and AuNPs played a role in the enhanced photodynamic effect of ZnO/CuO. Therefore, based on these results, the intracellular generation of ROS resulted from a_m-ZnO@CuO@Au HNSs inside the cancer cells under irradiation, which further inhibited cell proliferation and induced cell apoptosis [42].

2.3 Photothermal property of a_m-ZnO@CuO@Au HNSs

The optical property of a_m-ZnO@CuO@Au HNSs aqueous solution was studied via UV-vis-NIR spectroscopy (Figure S14). a_m-ZnO@CuO@Au HNSs exhibited broad and strong absorption ranging from UV to visible wavelengths. The broad and strong red emission made a_m-ZnO@CuO@Au HNSs as highly promising photothermal agent for PTT. Therefore, their photothermal conversion efficiency was evaluated, and a_m-ZnO@CuO@Au HNSs aqueous solutions with different concentrations were irradiated under 635 nm laser (2.0 W/cm^2, 5 min). The results indicated that temperatures of a_m-ZnO@CuO@Au HNSs solutions increased with the irradiation time (Figure 3A), and the solutions with high concentrations showed a rapid increase in temperature. After irradiation for 5 min, the temperature of a_m-ZnO@CuO@Au HNSs aqueous solution with a concentration of 200 μg/mL was increased by 51.1 °C (Figure 3B) under 2.0 W/cm^2 irradiation, whereas that of the a_m-ZnO@CuO@Au HNSs aqueous solution was kept constant with 0.1 W/cm^2. Then, the measurement of the photothermal conversion efficiency (η) of a_m-ZnO@CuO@Au HNSs solution was carried out to further evaluate their photothermal conversion ability (Figure 3C, D). The η value was calculated according to the previously reported model [43], and the η value of a_m-ZnO@CuO@Au HNSs was 26.9%. The high η value of a_m-ZnO@CuO@Au HNSs made them a promising photothermal coupling agent.

2.4 Preparation of RGD@a_m-ZnO@CuO@Au@DOX

We synthesized the RGD@a_m-ZnO@CuO@Au@DOX for targeting cancer cells, dissolving Zn^{2+}/Cu^{2+} ions, red-light or pH-triggered drug release, PTT, and PDT. As we know, RGD is an ideal targeting molecule for cancer cells, and RGD overexpression is related to disease progression and cancer cell survival [44]. RGD was covalently grafted with PEGylated HNSs via an activated amide coupling to obtain RGD@HNSs. PEGylated HNSs were obtained by the passivation reaction. The remaining terminal -NH_2 groups of the PEG moiety were available for loading the RGD into the nanocomposites. PEG was successfully loaded onto the surface of the HNSs, as shown in FT-IR (Figure S15). DOX was chosen as a model drug to test a_m-ZnO@CuO@Au HNSs drug delivery system because DOX is an effective anticancer drug at very low concentrations. RGD@a_m-ZnO@CuO@Au@DOX HNSs had three functions as follows: (1) targeting cancer cells via the RGD, PDT, and PTT by red-light irradiation, (2) dissolving Zn^{2+}/Cu^{2+} ions by the tumor microenvironment, and (3) anticancer drug delivery by using the hollow interior. Therefore, the targeted cancer cells were affected by Zn^{2+}/Cu^{2+}, PDT, and PTT effects, and the drug was released at the same time. For biological applications, stability under physiological conditions is crucial. As illustrated in inset of Figure 3E, the RGD@a_m-ZnO@CuO@Au@DOX HNSs exhibited high stability in physiological mediums, including water, phosphate buffered solution (PBS), and Dulbecco's modified Eagle medium (DMEM).

We speculated that DOX was loaded into RGD@a_m-ZnO@CuO@Au HNSs using Zn^{2+}-DOX chelate complex formation [23]. The drug loading was confirmed by UV-vis and fluorescence spectroscopy, as shown in Figure 3E. Compared with the free DOX, the loaded DOX showed a slight red shift in the absorption. Furthermore, the fluorescence of DOX was quenched slightly after loading into RGD@a_m-ZnO@CuO@Au HNSs. However, only a slight fluorescence quenching was observed when DOX was mixed with RGD@a_m-ZnO@CuO@Au HNSs (Figure

3F), excluding the possibility of inner filter effect. The data confirm that the formation of RGD@a_m-ZnO@CuO@Au@DOX HNSs occurred. We also measured the DOX loading capacities with increasing DOX concentrations (Figure 3G). Their loading efficiency was calculated to be 187% (DOX: RGD@a_m-ZnO@CuO@Au HNSs, w/w). This amount was one of the largest reported in terms of drug loading capacity for a drug delivery vehicle system based on HNSs.

2.5 DOX releasing

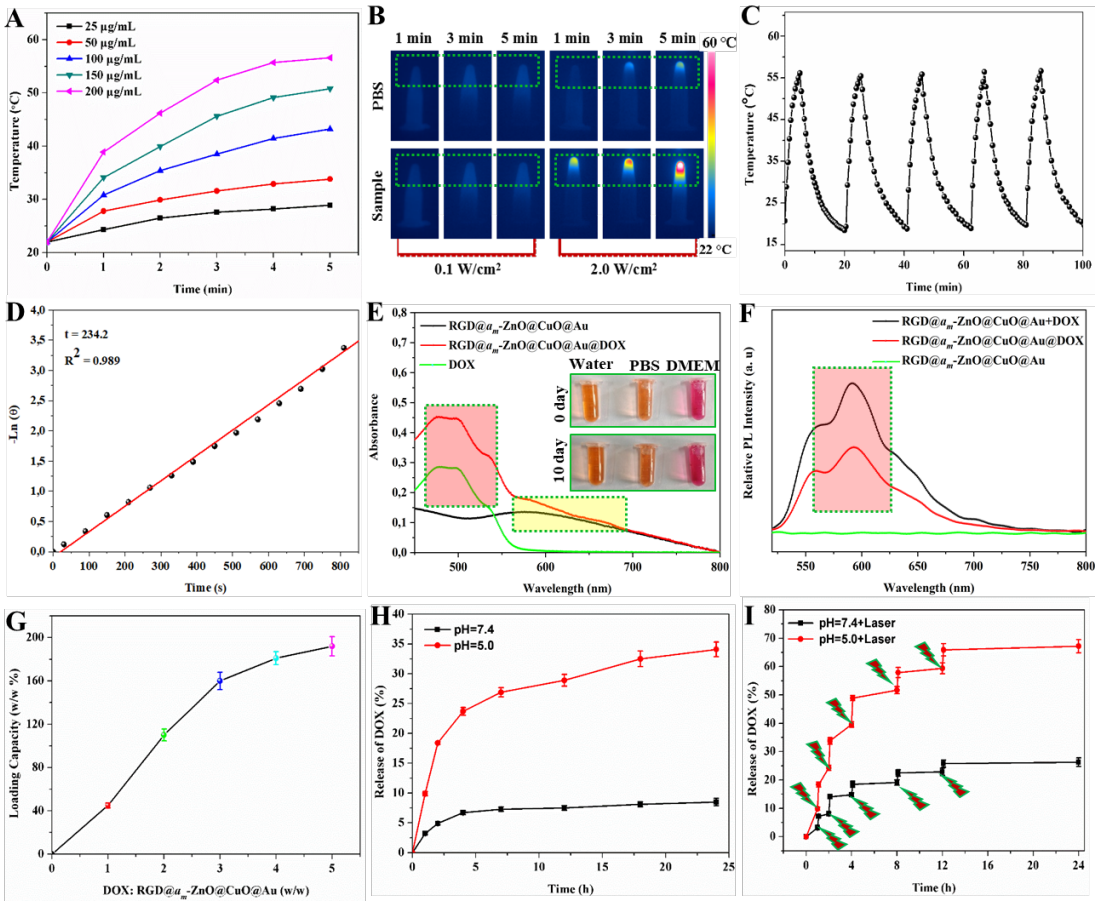

Figure 3. (A) Temperature elevation of different concentrations of a_m-ZnO@CuO@Au HNSs under irradiation with 635 nm laser. (B) Photothermal images of a_m-ZnO@CuO@Au HNSs solutions at different laser power and irradiation time. (C) Temperature changes of a_m-ZnO@CuO@Au HNSs solutions under irradiation at 635 nm laser (2.0 W/cm^2, 5 cycles). (D) Linearity curves fitted from the -ln(θ) vs temperature cooling time of (C). (E) UV-vis-NIR spectroscopy of RGD@a_m-ZnO@CuO@Au, RGD@a_m-ZnO@CuO@Au@DOX HNSs, and DOX. Inset is the stability of the RGD@a_m-ZnO@CuO@Au@DOX HNSs in physiological mediums. (F) Fluorescence spectra of RGD@a_m-ZnO@CuO@Au+DOX, RGD@a_m-ZnO@CuO@Au, and RGD@a_m-ZnO@CuO@Au@DOX HNSs. (G) DOX loading

capacity of RGD@a_m-ZnO@CuO@Au HNSs at various DOX concentrations. (H) DOX release from RGD@a_m-ZnO@CuO@Au@DOX HNSs at different pH values. (I) Red-light-triggered release of DOX from RGD@a_m-ZnO@CuO@Au@DOX HNSs.

The release profile of DOX from RGD@a_m-ZnO@CuO@Au@DOX HNSs at different pH values was studied, as shown in Figure 3H. The amount of released DOX was analyzed via UV-Vis spectrum [45]. After incubation for 24 h, approximately 33.4% of DOX released from HNSs under pH 5.0 compared with only 7.7% of DOX released under pH 7.4. This result implied that pH-triggered release was due to increased protonation of -NH_2 groups in the DOX in an acidic medium. We then wondered whether red-light-induced photothermal could also trigger DOX release from HNSs. RGD@a_m-ZnO@CuO@Au@DOX HNSs in PBS (pH 5.0 and 7.4) were irradiated by the 635 nm laser (2.0 W/cm^2, 5 min), as shown in Figure 3I. Compared with DOX released in the dark, the DOX release with red-light-stimulus was dramatically enhanced. With the same laser irradiation, the DOX release seemed to be obvious highly at the low pH value compared with that under the physiological pH. However, compared with DOX releasing in the dark, its performance triggered by red-light enhanced apparently at different pH, indicating that the DOX release amount could be further increased under laser irradiation due to the PTT effect of RGD@a_m-ZnO@CuO@Au@DOX HNSs.

2.6 Hemolysis assay of the RGD@a_m-ZnO@CuO@Au@DOX HNSs

Hemolysis has been widely used in the biosafety assessment of various biomedical nanomaterials [46]. As shown in Figure 4A, no significant hemolysis (<5%) was observed when RGD@a_m-ZnO@CuO@Au@DOX HNSs were co-cultured with RBCs. The morphologically aberrant forms of RBCs could always serve as a distinct explanation for the diagnosis of various medical conditions, including hemolytic anemia. The photomicrographs from Figure 4B indicated that the treatment of RGD@a_m-ZnO@CuO@Au@DOX HNSs did not alter the shape and number of RBCs in the test mice. The *in vitro* biocompatibility study provided practical data for the clinical applications of our HNSs.

2.7 In vitro targeted cancer cells

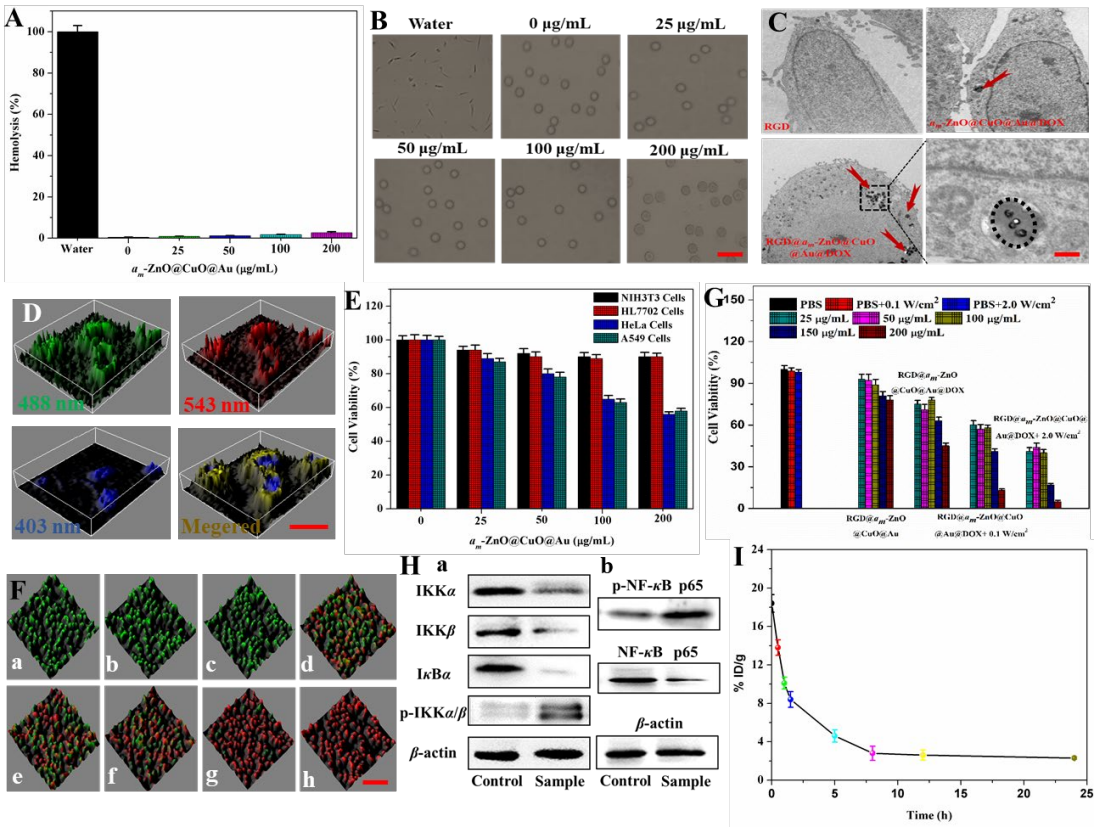

Figure 4. (A) Hemolytic assay of RGD@a_m-ZnO@CuO@Au@DOX HNSs. (B) Optical images of RBCs treated with RGD@a_m-ZnO@CuO@Au@DOX HNSs. Scale bars: 20 μm. (C) TEM images of A549 cells after RGD@a_m-ZnO@CuO@Au@DOX HNSs treatment. Scale bars: 1 μm. (D) Colocalization analysis of RGD@a_m-ZnO@CuO@Au@DOX HNSs in A549 cells. Scale bars: 20 μm. (E) Relative viability of various cells treated with different concentrations of RGD@a_m-ZnO@CuO@Au HNSs. (F) Fluorescence images of calcein-AM/PI-stained A549 cells treated with various media. Scale bars: 100 μm. (G) Relative viability of A549 cells treated with different concentrations of RGD@a_m-ZnO@CuO@Au@DOX HNSs under different conditions. (H) The expression of NF-κB activation-related proteins after RGD@a_m-ZnO@CuO@Au@DOX HNSs incubation for 48 h. (I) The blood circulation of RGD@a_m-ZnO@CuO@Au@DOX HNSs after injection.

The binding affinity of a_m-ZnO@CuO@Au was examined against A549 cells by measuring the Au element concentration to verify the targeting ability of a_m-ZnO@CuO@Au against RGD on the surface of cancer cells. RGD@a_m-ZnO@CuO@Au@DOX HNSs bound to A549 cells with an approximately 2.5-fold higher affinity than that of a_m-ZnO@CuO@Au HNSs (Figure S16). The

successful internalization of RGD@a_m-ZnO@CuO@Au@DOX HNSs into A549 cells via receptor-mediated endocytosis was observed via sectional TEM. The sectional TEM image in Figure 4C confirmed that RGD@a_m-ZnO@CuO@Au@DOX HNSs accumulated in tumor cells and were mostly distributed uniformly throughout the cytoplasm. Co-staining studies with Lyso-Tracker Green and Hoechst33342 were performed to further identify the intracellular locations of RGD@a_m-ZnO@CuO@Au@DOX. As shown in Figure 4D, A549 cells treated with RGD@a_m-ZnO@CuO@Au@DOX HNSs showed punctuate bright red fluorescence, which overlaid well with the green fluorescence from the lysosomal tracker. This phenomenon implied that RGD@a_m-ZnO@CuO@Au@DOX HNSs accumulated mainly in the lysosomes of A549 cells.

2.8 Cytotoxicity assay

Besides, the assessment of cell viability of different cell lines was examined. RGD@a_m-ZnO@CuO@Au HNSs did not cause cytotoxicity to both human lung (MRC-5) and mouse embryonic fibroblasts (NIH3T3) cell lines even at concentration as high as 200 μg/mL (Figure 4E). However, the cytotoxicity effect became significant by using cancer cell lines, such as human cervical carcinoma (HeLa) and A549 cell lines. This pronounced cytotoxicity to cancer cells was due to the accelerated dissolution of free Zn^{2+}/Cu^{2+} in the tumor environment, which was consistent with the previous researches [23,25]. Next, we studied the multimodal Zn^{2+}/Cu^{2+} therapy, chemotherapy, PDT, and PTT efficacy and cytotoxicity of the prepared RGD@a_m-ZnO@CuO@Au@DOX HNSs *in vitro*. Live and dead cells could be differentiated by using calcein-AM and PI co-staining methods. In the PBS (Figure 4F,a), 0.1 W/cm^2 laser (Figure 4F,b), and 2.0 W/cm^2 laser (Figure 4F,c), no cell death was found because all cells displayed green fluorescence. This phenomenon illustrated the inability of the heat generated from the pure medium under laser irradiation to cause cancer cell death. Parts of the cells were destroyed after RGD@a_m-ZnO@CuO@Au HNSs incubation (Figure 4F,d), free DOX (Figure 4F,e),

and RGD@a_m-ZnO@CuO@Au@DOX HNSs (Figure 4F,f). Moreover, upon 0.1 W/cm^2 laser irradiation (Figure 4F,g), the majority of the cells were destroyed after RGD@a_m-ZnO@CuO@Au@DOX HNSs incubation because of the ease with which Zn^{2+}/Cu^{2+}, DOX, and $^1O_2$ were produced and the inability to generate heat under low laser power doses. However, upon 2.0 W/cm^2 laser irradiation (Figure 4F,h), all cells were essentially killed, as indicated by the intense red fluorescence. These results suggested that RGD@a_m-ZnO@CuO@Au@DOX HNSs could simultaneously generate Zn^{2+}/Cu^{2+}, DOX, $^1O_2$, and produce heat to efficiently kill cells via simultaneous Zn^{2+}/Cu^{2+} therapy, chemotherapy, PDT, and PTT by using a single red-light laser. MTT assay in there was further applied to evaluate the cytotoxicity and multimodal Zn^{2+} therapy, chemotherapy, PDT, and PTT efficacy of RGD@a_m-ZnO@CuO@Au@DOX HNSs. In the Zn^{2+} therapy, chemotherapy, PDT, and PTT groups (2.0 W/cm^2), cell viability drastically decreased as the RGD@a_m-ZnO@CuO@Au@DOX HNSs concentration increased from 100 μg/mL to 200 μg/mL (Figure 4G). A mortality rate of 98% was obtained, indicating that the simultaneous effects of Zn^{2+}/Cu^{2+} therapy, chemotherapy, PDT, and PTT can efficiently kill cancer cells. This result agreed with findings from calcein AM and PI co-staining. Therefore, the prepared RGD@a_m-ZnO@CuO@Au@DOX HNSs featured targeting cancer cells, pH-induced dissolution to Zn^{2+}/Cu^{2+} ions, efficient red-light/pH-induced releasing DOX, and efficient red-light-induced generation of $^1O_2$ and heat.

2.9 Inhibition of NF-κB activation

It is well known that the activation of NF-κB is closely associated with ROS generation, tumorigenesis and apoptosis, so we monitored the expression of several related proteins activated by the transcription factor (NF-κB) [47]. We found that the p-IKKα/β expression levels showed a sharply increase after exposure to RGD@a_m-ZnO@CuO@Au@DOX HNSs upon 635 nm laser for 48 h, suggesting the activated state of NF-κB (Figure 4H,a). Also, the increased nucleus p-NF-κB p65

expression levels and the decreased nucleus NF-κB p65 expression levels were found in A549 cells (Figure 4H,b). This result indicated that RGD@a_m-ZnO@CuO@Au@DOX HNSs led to the activation of NF-κB, in the form of fostering the formation of p-IKKα/β, following the degradation of IκBα, and further causing NF-κB phosphorylation and transfer into the nucleus, which might further initiated the expression of some apoptotic genes like tumor necrosis factor α. Thus, the ROS-mediated NF-κB activation played an important role in RGD@a_m-ZnO@CuO@Au@DOX HNSs-induced cell apoptosis.

2.10 Blood circulation

Before the *in vivo* study of tumor combination therapy by using RGD@a_m-ZnO@CuO@Au@DOX HNSs, we studied the *in vivo* behavior of such agents in animals by utilizing the intrinsic physical properties of DOX. Blood was extracted from Balb/c mice at different time points after intravenous injection. The concentrations of RGD@a_m-ZnO@CuO@Au@DOX HNSs in the blood were determined by measuring the UV signals (480 nm) of DOX. As shown in Figure 4I, the blood level of RGD@a_m-ZnO@CuO@Au@DOX HNSs decreased gradually over time. However, the RGD@a_m-ZnO@CuO@Au@DOX HNSs in the blood remained at a relatively high level even at 24 h after injection.

2.11 In vivo fluorescence and MR imaging

Among the various kinds of metal ions, Cu^{2+} could be utilized as a contrast agent for MR imaging [45]. As expected, a distinct concentration-dependent brightening effect was observed in *in vitro* T_1-weighted MR images of RGD@a_m-ZnO@CuO@Au@DOX HNSs, indicating its potential use in T_1-weighted MR imaging (Figure 5A). After the intravenous injection of RGD@a_m-ZnO@CuO@Au@DOX HNSs into A549 tumor-bearing mice, a remarkably brightened appearance was observed in the tumor region of mice from *in vivo* MR imaging, suggesting high tumor accumulation of those NPs after systemic

administration (Figure 5B). The quantitative MR imaging results further verified that the T_1 signals were decreased in the tumor region after intravenous injection of RGD@a_m-ZnO@CuO@Au@DOX HNSs for 6 h (Figure 5C).

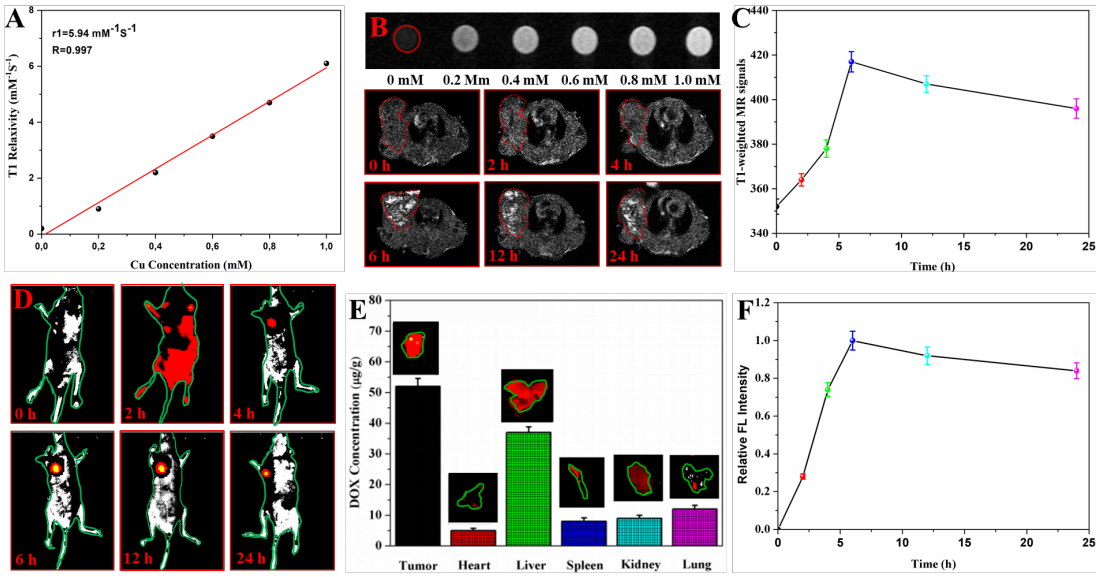

Figure 5. (A) T_1 relaxation rates of RGD@a_m-ZnO@CuO@Au@DOX HNSs at different Cu^{2+} concentrations. (B) Time-dependent T_1-weighted MR images of the mouse before and 2, 4, 6, 12 and 24 h post-injection of RGD@a_m-ZnO@CuO@Au@DOX HNSs. (C) Average T_1-weighted MR intensities from the tumor sites after 24 h injection. (D) *In vivo* fluorescence imaging of the mouse at different time points after intravenous injections. (E) *Ex vivo* images of mice tissues. (F) Average fluorescence intensities from the tumor sites after 24 h injection.

Fluorescence imaging was performed to clarify the body distribution of RGD@a_m-ZnO@CuO@Au@DOX HNSs. Figure 5D revealed that the RGD@a_m-ZnO@CuO@Au@DOX HNSs accumulated in the tumor sites through the enhanced permeability and retention (EPR) and RGD-targeted effect. After 24 h post-injection, the mice were sacrificed and their major organs and tumor were excised and imaged to evaluate accumulation amount. RGD@a_m-ZnO@CuO@Au@DOX HNSs mainly accumulated in the tumor and liver tissues (Figure 5E), similar to the previous literature [48]. The kidneys and lung tissue showed stronger fluorescence intensity than that of the spleen and heart. Then, the time-dependent accumulation of RGD@a_m-ZnO@CuO@Au@DOX HNSs in the tumor sites was further quantified (Figure 5F). The average fluorescence intensity of RGD@a_m-ZnO@CuO@Au@DOX HNSs in the tumor sites rapidly increased within

2–6 h post-injection, reaching a plateau within 6–12 h post-injection, and slowly decreased over time. Incorporating these findings, 6 h was chosen as a proper time to carry out cancer treatment. Therefore, *in vivo* MR and fluorescence imaging confirmed the efficient tumor targeting of RGD@a_m-ZnO@CuO@Au@DOX HNSs after intravenous injection.

2.11 In vivo photothermal imaging and synergistic therapy

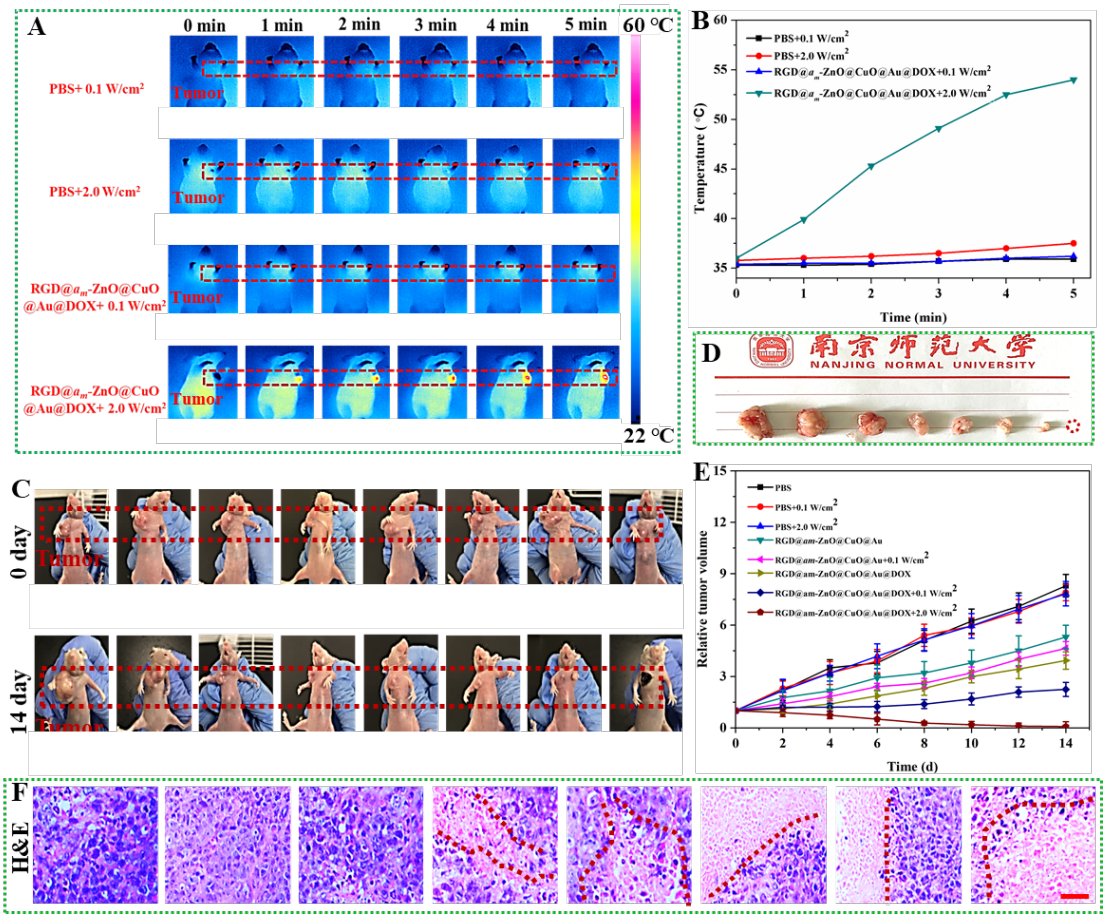

Figure 6. (A) Thermographs of A549 tumor-bearing mice under 635 nm laser irradiation (2.0 or 0.1 W/cm^2, 5 min). (B) Time-dependent temperature changes of the tumors during laser irradiation. (C) Representative photographs of mice and (D) excised tumors from different groups. (E) Relative tumor volume of tumor-bearing mice with different treatments. (F) H&E stained images of tumor slices with different treatments. Scale bars: 150 μm. The groups in the order from left to right in (C), (D), and (F) are as follows: PBS, PBS+0.1 W/cm^2, PBS+2.0 W/cm^2, RGD@a_m-ZnO@CuO@Au NHSs, RGD@a_m-ZnO@CuO@Au NHSs+0.1 W/cm^2, RGD@a_m-ZnO@CuO@Au@DOX NHSs, RGD@a_m-ZnO@CuO@Au@DOX NHSs+0.1 W/cm^2, and RGD@a_m-ZnO@CuO@Au@DOX NHSs+2.0 W/cm^2.

Inspired by the attractive *in vitro* synergistic therapeutic effect and the excellent tumor accumulation of RGD@a_m-ZnO@CuO@Au@DOX HNSs, we conducted animal experiments to realize the Zn^{2+}/Cu^{2+} therapy, chemotherapy, and PTT *in vivo* with RGD@a_m-ZnO@CuO@Au@DOX HNSs. As a proof-of-concept experiment, A549 tumor modal on nude mice were divided into different groups (n = 5) and intravenously injected with RGD@a_m-ZnO@CuO@Au@DOX HNSs and PBS. At 6 h intravenous, partial tumors were irradiated with the 635 nm laser at a moderate power density of 0.1 or 2.0 W/cm^2 for 5 min. An IR thermal camera was used to monitor the tumor temperature (Figure 6A). The tumor surface temperatures of mice treated with RGD@a_m-ZnO@CuO@Au@DOX HNSs rapidly increased and was maintained at 50 °C during laser irradiation (Figure 6B). By contrast, the mice treated with PBS did not show apparent temperature rise in the tumor region during laser irradiation.

We then studied the *in vivo* therapeutic efficacy of RGD@a_m-ZnO@CuO@Au@DOX HNSs. After receiving different treatments, the tumor sizes were measured every 2 d. Noticeably, the tumor growths on mice with RGD@a_m-ZnO@CuO@Au@DOX HNSs injection were effectively inhibited after red-light laser irradiation as a result of synergistic therapy (Figure 6C-E). The mice in the RGD@a_m-ZnO@CuO@Au@DOX HNSs, RGD@a_m-ZnO@CuO@Au HNSs+0 or 0.1 W/cm^2, and RGD@a_m-ZnO@CuO@Au@DOX HNSs+0.1 W/cm^2 groups notably showed only a slight delay in tumor growth, suggesting that these therapies were insufficient to kill tumor cells completely. In the three control groups (PBS, PBS+0.1 W/cm^2, or PBS+2.0 W/cm^2), tumors quickly grew within the test period, and no significant body weight variations were observed after treatment. The tumors were also collected for hematoxylin and eosin (H&E) staining 1 d after treatment (Figure 6F). No change was observed in the control groups (PBS, PBS+0.1 W/cm^2, or PBS+2.0 W/cm^2). In the RGD@a_m-ZnO@CuO@Au@DOX HNSs, RGD@a_m-ZnO@CuO@Au HNSs+0.1 W/cm^2, and RGD@a_m-ZnO@CuO@Au@DOX HNSs+0.1 W/cm^2 group, some inflammatory cell

infiltrations and cell death might be observed. In the RGD@a_m-ZnO@CuO@Au@DOX HNSs+2.0 W/cm^2 group, all cancer cells were damaged. The breakdown of the nuclear membrane and shrinkage of nuclei with karyorrhexis and pyknosis were further detected.

No obvious change was found in the bodyweight of all groups (Figure S17), suggesting that RGD@a_m-ZnO@CuO@Au@DOX HNSs did not have any toxicity to the body of mice. The major organs of the mice were sliced and stained by H&E for histology analysis to further evaluate the therapeutic efficacy and the *in vivo* toxicity of RGD@a_m-ZnO@CuO@Au@DOX HNSs. The major organs were collected from the mice after treatment (Figure S18). No evident damage or inflammation was observed compared with the control groups. The serum biochemistry tests also performed for quantitative evaluation of three important hepatic indicators and two kidney function indicators [49]. The resulting data shown in Figure S19 revealed that these indicators were at similar levels for the mice exposed to RGD@a_m-ZnO@CuO@Au@DOX HNSs and for the control mice. These results indicated that RGD@a_m-ZnO@CuO@Au@DOX HNSs had red-light-triggered cancer theranostic functions for Zn^{2+}/Cu^{2+} therapy, chemotherapy, and phototherapy *in vivo*.

3. Conclusions

In summary, we designed a new multifunctional nanoplatform based on multi-shelled hollow spheres for imaging-guided synergistic cancer treatment. The developed RGD@a_m-ZnO@CuO@Au@DOX HNSs possessed the following features: (1) cancer cells targeting, (2) efficient ROS generation and high photothermal conversion efficiency under 635 nm laser irradiation, (3) reduction to Zn^{2+}/Cu^{2+} by acidic endosomes/lysosomes, and (4) red-light/pH-triggered cancer theranostics, which enabled simultaneous imaging-guided Zn^{2+}/Cu^{2+} therapy, chemotherapy, and phototherapy. A good understanding of the *in vivo* behavior of as-obtained RGD@am-ZnO@CuO@Au@DOX HNSs, such as their quantitative

pharmacokinetics, biodistribution and long-term toxicity, is of importance and requires further exploration. The RGD@a_m-ZnO@CuO@Au@DOX HNSs opens a new therapeutic window for the treatment of cancer and stands out as a cost-effective theranostic reagent in the field of nanomedicine.

Acknowledgments

This project was supported by the Foundation of Jiangsu Collaborative Innovation Center of Biomedical Functional Materials, the Jiangsu province science and technology support plan (BE2015367), and the Villum Fonden, Denmark, Project No. 13153. B.S., M.Z., and T.Z. thanks the China Scholarship Council (CSC) for generous support.

Conflicts of interest

The authors have no existing conflicts to declare.

References

[1] R. R. Xing, K. Liu, T. F. Jiao, N. Zhang, K. Ma, R.Y. Zhang, Q. L. Zou, G. H. Ma and X. H. Yan, *Adv. Mater.*, 2016, **28**, 3669-3676.
[2] K. Wu, H. H. Zhao, Z. Q. Sun, B. Wang, X. Y. Tang, Y. N. Dai, M. X. Li, Q. M. Shen, H. Zhang, Q. L. Fan, W. Huang, *Theranostics*, 2019, **9**, 7697-7713.
[3] L. Cheng, C. Wang, L. Z. Feng, K. Yang and Z. Liu, *Chem. Rev.*, 2014, **114**, 10869-10939.
[4] J. C. Ge, Q. Y. Jia, W. M. Liu, M. H. Lan, B. J. Zhou, L. Guo, H. Y. Zhou, H. Y. Zhang, Y. Wang, Y. Gu and X. M. Meng, *Adv. Healthcare Mater.*, 2016, **5**, 665-675.
[5] M. Zhang, W. T. Wang, F. Wu, P. Yuan, C. Chi and N. L. Zhou, *Carbon*, 2017, **123**, 70-83.
[6] D. Yang, G. X. Yang, P. P. Yang, R. C. Lv, S. L. Gai, C. X. Li, F. He and J. Lin, *Adv. Funct. Mater.*, 2017, **27**, 1700371.
[7] S. Liang, Z. X. Xie, Y. Wei, Z. Y. Cheng, Y. Q. Han and J. Lin, *Dalton Trans.*, 2018, **47**, 7916-7924..
[8] C. Liang, L. G. Xu, G. S. Song, Z. Liu, *Chem. Soc. Rev.*, 2016, **45**, 6250-6269.
[9] X. R. Song, X. Y. Wang, S. X. Yu, J. B. Cao, S. H. Li, J. Li, G. Liu, H. H. Yang and X. Y. Chen, *Adv. Mater.*, 2015, **27**, 3285-3291.
[10] L. Jiang, Z. M.Gao, L. Ye, A. Y. Zhang and Z. G. Feng, *Biomater. Sci.*, 2013, **1**, 1282-1291.
[11] S. H. Sun, S. J. Sun, Y. Sun, P. Wang, J. L. Zhang, W. J. Du, S. M, Wang and X. L. Liang, *Theranostics,* 2019, **9**, 8138-8154.
[12] C. C. Wang, L. C. Liu, H. L. Cao and W. A. Zhang, *Biomater. Sci.*, 2017, **5**, 274-284.

[13] L. Cheng, C. Yuan, S. D. Shen, X. Yi, H. Gong, K. Yang and Z. Liu, *ACS nano*, 2015, **9**, 11090-11101.
[14] T. F. Zhu, X. Q. Ma, R. H. Chen, Z. J. Ge, J. Xu, X. K. Shen, L. Jia, T. Zhou, Y. F. Luo and T. L. Ma, *Biomater. Sci.*, 2017, **5**, 1090-1100.
[15] S. G. Wang, K. Li, Y. Chen, H. R. Chen, M. Ma, J. W. Feng, Q. H. Zhao and J. L. Shi, *Biomaterials*, 2015, **39**, 206-217.
[16] R. Sivaraj, P. K. S. M. Rahman, P. Rajiv, S. Narendhran and R. Venckatesh, *Spectrochim. Acta Part A*, 2014, **129**, 255-258.
[17] Q. H. Feng, Y. Y. Zhang, W. X. Zhang, Y. W. Hao, Y. C. Wang, H. L. Zhang, L. Hou and Z. Z. Zhang, *Acta Biomater.*, 2017, **49**, 402-413.
[18] Z. Y. Zhang, H. Suo, X. Q. Zhao, D. Sun, L. Fan and C. F. Guo, *ACS Appl. Mater. Interfaces*, 2018, **10**, 14570-14576.
[19] T. Zheng, T. C. Zhou, X. T. Feng, J. Shen, M. Zhang and Y. Sun, *ACS Appl. Mater. Interfaces*, 2019, **11**, 31615-31626
[20] Z. Kang, X. Q. Yan, L. Q. Zhao, Q. L. Liao, K. Zhao, H. W. Du, X. H. Zhang, X. J. Zhang and Y. Zhang, *Nano Res.*, 2015, **8**, 2004-2014.
[21] W. Zheng, M. Wei, S. Li and W. D. Le, *Nanomedicine*, 2016, **11**, 1417-1430.
[22] M. V. Yezhelyev, X. H. Gao, Y. Xing, A. Al-Hajj, S. Nie and R. M. O'Regan, *Lancet Oncol.*, 2006, **7**, 657-667.
[23] X. L. Cai, Y. N. Luo, W. Y. Zhang, D. Du and Y. H. Lin, *Appl. Mater. Interfaces*, 2016, **8**, 22442-22450.
[24] M. K. K. Oo, Y. Yang, Y. Hu, M. Gomez, H. Du, H. J. Wang, *ACS nano*, 2012, **6**, 1939-1947.
[25] N. Waiskopf, Y. Ben-Shahar, M. Galchenko, I. Carmel, G. Moshitzky, He. Soreq and U. Banin, *Nano Lett.*, 2016, **6**, 4266-4273.
[26] X. S. Zhao, X. Ren, R. Zhu, Z. Luo and B. Ren, *Aquat. Toxicol.*, 2016, **180**, 56-70.
[27] C. Ng, L. Q. Yong, M. P. Hande, C. N. Ong, L. E. Yu, B. H. Bay and Gy. H. Baeg, *Int. J. Nanomed.*, 2017, **12**, 1621-1637.
[28] P. Sivakumar, M. Lee, Y. Kim and M. S. Shim, *J. Mater. Chem. B*, 2018, **6**, 4852-4871.
[29] K. Gold, B. Slay, M. Knackstedt and A. K. Gaharwar, *Adv. Ther.,* 2018, 1, 1700033.
[30] W. W. He, H. Kim, W. G. Wamer, D. Melka, J. H. Callahan and J. Yin, *J. Am. Chem. Soc.*, 2013, **136**, 750-757.
[31] M. Zhang, F. Wu, W. T. Wang, J. Shen, N. L. Zhou and C. Z. Wu, *Chem. Mater.*, 2018, **31**, 1847-1859.
[32] J. Gupta, P. Bhargava and D. Bahadur, *J. Mater. Chem. B,* 2015, **3**, 1968-1978.
[33] W. B. Wu, D. Mao, X. L. Cai, Y. K. Duan, F. Hu, D. L. Kong and B. Liu, *Chem. Mater.*, 2018, **30**, 3867-3873.
[34] P. K. Jain, K. Manthiram, J. H. Engel, S. L. White, J. A. Faucheaux and A. P. Alivisatos, *Angew. Chem.*, 2013, **125**, 13916-13920.
[35] Y. Chang, Y. Cheng, Y. L. Feng, H. Jian, L. Wang, X. M. Ma, X. Li and H. Y. Zhang, *Nano Lett.*, 2018, **18**, 886-897.
[36] N. Karim, M. Singh, P. Weerathunge, P. Bian, R. K. Zheng, C. Dekiwadia, T. Ahmed, S. Walia, E. D. Gaspera, S. Singh, R. Ramanathan and V. Bansal, *ACS Appl. Mater. Interfaces*, 2018, **1**, 1694-1704.
[37] T. Pandiyarajan, R. Saravanan, B. Karthikeyan, F. Gracia, Héctor D. Mansilla, M. A.

Gracia-Pinilla and R. V. Mangalaraja, *J. Mater. Sci.: Mater. Electron.,* 2017, **28**, 2448-2457.
[38] C. Tao, L. An, J. M. Lin, Q. W. Tan, S. P. Yang. *Small*, 2019, **15**, 1903473.
[39] Y. Chang, M. Y. Zhang, L. Xia, J. Zhang and G. Xing, *Materials,* 2012, **5**, 2850-2871.
[40] R. Ge, M. Lin, X. Li, S. W. Liu, W. J. Wang, S. Y. Li, X. Zhang, Y. Liu, L. D. Liu, F. Shi, H. C. Sun, H. Zhang and B. Yang, *ACS Appl. Mater. Interfaces*, 2017, **9**, 19706-19716.
[41] G. Zhan and H. C. Zeng, *Chem. Mater.*, 2017, **29**, 10104-10112.
[42] H. Wang, X. Z. Yang, W. Shao, S. C. Chen, J. F. Xie, X. D. Zhang, J. Wang and Y. Xie, *J. Am. Chem. Soc.*, 2015, **137**, 11376-11382.
[43] S. L. Li, Y. H. Chen, H. B. Liu, Y. X. Wang, L. B. Liu, F. T. Lv, Y. L. Li and S. Wang, *Chem. Mater.*, 2017, **29**, 6087-6094.
[44] H. Shi, R. Q. Yan, L. Y. Wu, Y. D. Sun, S. Liu, Z. Y. Zhou, J. He and D. J. Ye, *Acta Biomater.*, 2018, **72**, 256-265.
[45] A. Chen, J. Sun, S. Liu, L. Li, X. Peng and R. Zhang, *Biomater. Sci.*, 2019. 2020, Advance Article.
[46] J. T. Tan, N. Meng, Y. T. Fan, Y. T. Su, M. Zhang, Y. H. Xiao and N. L. Zhou, *Mater. Sci. Eng. C*, 2016, **61**, 681-687.
[47] R. Yuan, H. L. Xu, X. H. Liu, Y. Tian, C. Li, X. L. Chen, S. N. Su, I. Perelshtein, A. Gedanken and X. K. Lin, *ACS Appl. Mater. Interfaces*, 2016, **8**, 31806-31812.
[48] C. G. Qian, J. C. Yu, Y. L. Chen, Q. Hu, X. Z. Xiao, W. J. Sun, C. Wang, P. J. Feng, Q. Shen and Z. Gu, *Adv. Mater.*, 2016, **28**, 3313-3320.
[49] T. Zheng, W. T. Wang, F. Wu, M. Zhang, J. Shen and Y. Sun, *Theranostics*, 2019, **9**, 5035.